

AGN driven outflows in the OH absorber galaxy IRAS 19154+2704

C. Hekatelyne,^{1,2*} Thaisa Storchi-Bergmann,^{2†} Rogemar A. Riffel,^{3‡} Preeti Kharb,⁴ Claudia M. Cassanta³
 Andrew Robinson,⁵ Dinalva A. Sales⁶

¹ *Universidad Tecnológica, Polo Educativo Tecnológico Rivera, Ruta 5 km 496, CP 40000, Rivera, Uruguay*

² *Departamento de Astronomia, Universidade Federal do Rio Grande do Sul, 91501-970, Porto Alegre, RS, Brazil*

³ *Departamento de Física, CCNE, Universidade Federal de Santa Maria, 97105-900, Santa Maria, RS, Brazil*

⁴ *National Centre for Radio Astrophysics, Tata Institute of Fundamental Research, S. P. Pune University Campus, Post Bag 3, Ganeshkhind, Pune 411 007, India*

⁵ *School of Physics and Astronomy, Rochester Institute of Technology, 84 Lomb Memorial Drive, Rochester, NY 14623, USA*

⁶ *Instituto de Matemática, Estatística e Física, Universidade Federal do Rio Grande, Rio Grande 96203-900, Brazil*

Accepted XXX. Received YYY; in original form ZZZ

ABSTRACT

We present a two-dimensional study of the gas distribution, excitation and kinematics of the OH absorber galaxy IRAS 19154+2704 using Gemini GMOS-IFU observations. Its continuum image shows a disturbed morphology indicative of a past or on-going interaction. The ionised gas emission presents two kinematic components: a narrow ($\sigma \lesssim 300 \text{ km s}^{-1}$) component that may be tracing the gas orbiting in the galaxy potential and a broad ($\sigma \gtrsim 500 \text{ km s}^{-1}$) component which is produced by an Active Galactic Nucleus (AGN) driven outflow, with velocities reaching -500 km s^{-1} which may exceed the escape velocity of the galaxy. The emission-line ratios and BPT diagrams confirm that the gas excitation in the inner $\sim 2 \text{ kpc}$ is mainly due the AGN, while in regions farther away, a contribution from star formation is observed. We estimate a mass outflow rate of $\dot{M}_{\text{out}} = 4.0 \pm 2.6 M_{\odot} \text{ yr}^{-1}$ at a distance of 850 pc from the nucleus. The corresponding outflow kinetic power $\dot{E}_{\text{out}} = (2.5 \pm 1.6) \times 10^{42} \text{ erg s}^{-1}$, is only $3 \times 10^{-4} L_{\text{bol}}$ (the AGN luminosity), but the large mass-outflow rate, if kept for a $\sim 10 \text{ Myr}$ AGN lifecycle, will expel $\approx 10^8 M_{\odot}$ in ionised gas alone. This is the 6th of a series of papers in which we have investigated the kinematics of ULIRGS, most of which are interacting galaxies showing OH Megamasers. IRAS19154 shows the strongest signatures of an active AGN, supporting an evolutionary scenario: interactions trigger AGN that fully appear in the most advanced stages of the interaction.

Key words: galaxies:active – galaxies: ULIRGs – galaxies:kinematics and dynamics – galaxies:ISM

1 INTRODUCTION

The process of galaxy mergers and interactions is of paramount importance in the evolution of galaxies, as it leads to modifications in their morphologies, physical and chemical properties (e.g. Mihos 1995; Schwarzkopf & Dettmar 2000; Perez et al. 2011; Krabbe et al. 2014; Araujo et al. 2023). (Ultra)Luminous Infrared Galaxies (U)LIRGs – with infrared luminosities of $L_{\text{IR}} > 10^{11} L_{\odot}$ – are the result of complex processes involving the interactions and mergers of galaxies and symbolize a key phase in the evolutionary path of galaxies, during which the gravitational interactions from mergers exert tidal torques, channeling gaseous material into the heart of the galaxy (Soifer et al 1987; Sanders et al 1988). This process can trigger intense star formation (SF) and the fuelling an Active Galactic Nucleus (e.g. Tissera et al. 2002; Petric et al. 2018; Storchi-Bergmann & Schnorr-Müller 2019).

ULIRGs also appear to be the primary hosts of OH megamaser

(OHM) emitters, observed as a result of stimulated emission phenomena primarily emitting in the 1667 and 1665 MHz lines, with luminosities ranging from 10^2 to $10^4 L_{\odot}$ (Darling & Giovanelli 2000, 2002; Lo 2005). OHM galaxies may represent a short-lived transition phase during which dense concentrations of molecular gas trigger intense star formation episodes and the eruption of an AGN (Sanders et al 1988; Barnes & Hernquist 1992; Hopkins et al 2006; Haan et al 2011).

To better understand the relationship between ULIRGs, AGN SF, and OHM galaxies, we have an ongoing project dedicated to investigating the gas emission structure of a sample of roughly 70 galaxies selected from Darling & Giovanelli (2000), most of them with OHM emission. We use Hubble Space Telescope (HST) images, Very Large Array (VLA) observations and Integral Field Spectroscopy (IFS) data to characterize the gas emission-structure and kinematics in the inner few kiloparsec of these galaxies. The overall goal of our project is relating the merger stage and OH maser properties to quantitative measurements of AGN and Starburst activity. We have so far focused on a sub-sample of 15 galaxies for which we have HST broad band and ramp filter $H\alpha + [\text{NII}]$ observations (Sales et al 2015; Hekatelyne et al 2018a,b; Sales et al 2019; Hekatelyne

* E-mail: hekatelne.carpes@gmail.com (CH)

† E-mail: thaisa@ufrgs.br (TSB)

‡ E-mail: rogemar@ufsm.br (RAR)

et al 2020). This HST sample includes a range of merger stages and covers the redshift range $z = 0.009 - 0.26$, and a range of OH maser luminosities and OH line FWHM that are representative of the population of known OHMGs.

Our main results to date are summarized as follows. Sales et al (2015) concluded that the late-stage merger IRAS16399-0937 hosts an embedded AGN in one nucleus that is probably the source of the OHM emission observed in this system, while the second nucleus is starburst dominated. For IRAS F23199+0123, Hekatelyne et al (2018a) revealed an obscured type 2 AGN and reported a new OHM source related to the AGN. Also using multiwavelength observations, Hekatelyne et al (2018b) reported a possible embedded AGN in the midst of a circumnuclear ring of star formation in IRAS 03056+2034. Sales et al (2019) identified two kinematic components in IRAS 17526+3253 and concluded that the main source of ionization of this galaxy is young stars, although the presence of an AGN could not be discarded. And finally, Hekatelyne et al (2020) revealed that a faint AGN in IRAS 11506-3851 could be the origin of previously reported outflows in neutral and molecular gas. In summary, in our previous studies we have found five OHMs for which the GMOS-IFU data have resolved previously unknown AGNs and – although the number of objects is still small – our results support the hypothesis that OHM galaxies are hosts of AGNs that are being triggered by recent accretion of matter to their central Supermassive Black Hole (SMBH).

In this paper, we focus on a source with host properties similar to those of the galaxies previously studied, but with the OH feature observed in absorption. We present a detailed study of the ULIRG IRAS 19154+2704 (hereafter IRAS 19154), which has a redshift $z=0.0994$ (Nakanishi 1997), far infrared (FIR) luminosity $L_{FIR} 10^{10.66} L_{\odot}$ and is classified as an OH absorber by Darling & Giovannelli (2000). These authors reported that the 1665 MHz absorption line is strong and has a velocity in agreement with the auto-correlation function secondary peak and line separation predictions. Also, as reported by these authors, the host presents a fairly strong 1.4 GHz continuum with flux density of 64 mJy. Assuming the Hubble constant to be $H_0=70.5 \text{ km s}^{-1} \text{ Mpc}^{-1}$, and considering a distance of 436 Mpc, the adopted scale at the galaxy is $2.114 \text{ kpc arcsec}^{-1}$.

We use a combination of Gemini IFU data and HST images to map and study the gas distribution, kinematics and excitation in IRAS19154. In addition we present a 1.4 GHz continuum image obtained with the VLA. In section 2 we provide information on the observations and data reduction and in section 3 we describe the emission-line profile fitting and resulting gas distribution, excitation and kinematic results. In Section 4 we discuss the gas kinematics and the nature of the gas excitation and finally we present our conclusions in Section 5.

2 OBSERVATIONS AND DATA REDUCTION

2.1 GMOS-IFU data

The spectroscopic data of IRAS19154 were obtained at the Gemini North Telescope with the Gemini Multi Object Spectrograph (GMOS; Hook et al. 2004) operating in the Integral Field Unit (IFU) (Allington-Smith et al. 2002) mode. The GMOS-IFU data were obtained on the night of 2017 September 11, split into nine observations of 1180 seconds each, with the IFU operating in one slit mode using the grating B600-G5323 and the IFU-R mask. Moreover we obtained spectra centered at wavelengths 6200Å and 6300Å in order to allow recovery of the signal within the detector gaps.

Using this configuration, we obtained a field of view of $3.5'' \times 5.0''$ and recovered information from a spectral range that includes strong emission lines from $H\beta$ to $[S \text{ II}]\lambda 6731\text{Å}$. The data reduction followed the standard procedures for spectroscopic data and was performed using the GEMINI IRAF package. The basic steps of the reduction are the bias level subtraction, trimming and flat-fielding, wavelength calibration, sky subtraction and relative flux calibration, using observations of the standard star LTT 9239 performed at the same night of the observations of the galaxy.

As the final step, we median-combined the individual data cubes using the position of the peak of the continuum emission to perform the astrometry among the individual data cubes. We derived a seeing of 0.65 arcsec from the measurement of the full width at half maximum (FWHM) of the flux distribution of field stars available in the acquisition image obtained just before the observations of IRAS19154. The combined data cube covers the inner $3.4'' \times 5.0''$ of the galaxy at an angular sampling of $0.05'' \times 0.05''$.

Figure 1 shows, in the two upper rows, HST (left) and GMOS (right) images of IRAS19154, in the continuum (top) and in the $H\alpha+[N \text{ II}]$ emission lines (bottom). The two bottom rows, show two representative GMOS spectra: one centered on the position of the nucleus (labeled N) – defined as the location of the continuum peak – and the other from a location at ~ 2 arcsec east of the nucleus (labeled A). These spectra are integrated within an aperture radius of 0.3 arcsec. The strongest emission lines are identified in the nuclear spectrum and the comparison between the two spectra clearly reveals broader emission lines at the nucleus, compared to extranuclear regions.

2.2 GMOS-IFU Emission-line profile fitting

In order to obtain measurements of the gas properties in IRAS 19154 we used the IFSCUBE python package (Ruschel-Dutra 2020; Ruschel-Dutra et al. 2021) to model the emission-line profiles by Gaussian curves. We first use IFSCUBE to model the emission lines at the nucleus. By visual inspection of the spectra, we notice that a single Gaussian component can not reproduce the observed line profiles, as they usually present a broad wing in the nuclear region and thus, we include two Gaussian components per emission line. These components will be referred to as *broad* and *narrow* components, hereafter. We use the *cubefit* IFSCUBE module, providing as initial guesses for the centroid velocity and velocity dispersion (σ) the values obtained from the fits of the line profiles using the IRAF.SPLOT task, while the fluxes at the peak of the line profiles estimated directly with the IFSCUBE code are used as guesses for the Gaussian amplitudes. The fit of the emission-line profiles is performed in a continuum-subtracted cube, where the continuum emission is represented by a 5th order polynomial. These fits are performed from the nuclear spaxel outwards, following a spiral pattern. For each spaxel, initial guesses for the free parameters are provided as the values derived from successful fits of spaxels located at distances smaller than 0.15 arcsec.

The following emission lines are fitted simultaneously: $H\beta$, $[O \text{ III}] \lambda\lambda 4959, 5007$, $[O \text{ I}]\lambda\lambda 6300, 6364$, $[N \text{ II}] \lambda\lambda 6548, 6583$, $H\alpha$ and $[S \text{ II}] \lambda\lambda 6717, 6731$. The $[O \text{ III}]\lambda 5007/[O \text{ III}]\lambda 4959$ and $[N \text{ II}]\lambda 6583/[N \text{ II}]\lambda 6548$ line ratios are kept fixed to their theoretical values of 2.98 and 3.06, respectively (Osterbrock & Ferland 2006). The centroid velocity and velocity dispersion of emission lines from the same parent ions ($[O \text{ III}]$, $[N \text{ II}]$, $[S \text{ II}]$ and $H \text{ I}$) are kept tied, separately for the broad and narrow components.

Figure 2 shows examples of emission-line fits for the $H\beta+[O \text{ III}]\lambda\lambda 5007, 4959$ and $H\alpha+[N \text{ II}]\lambda\lambda 6548, 6583$ complexes for the

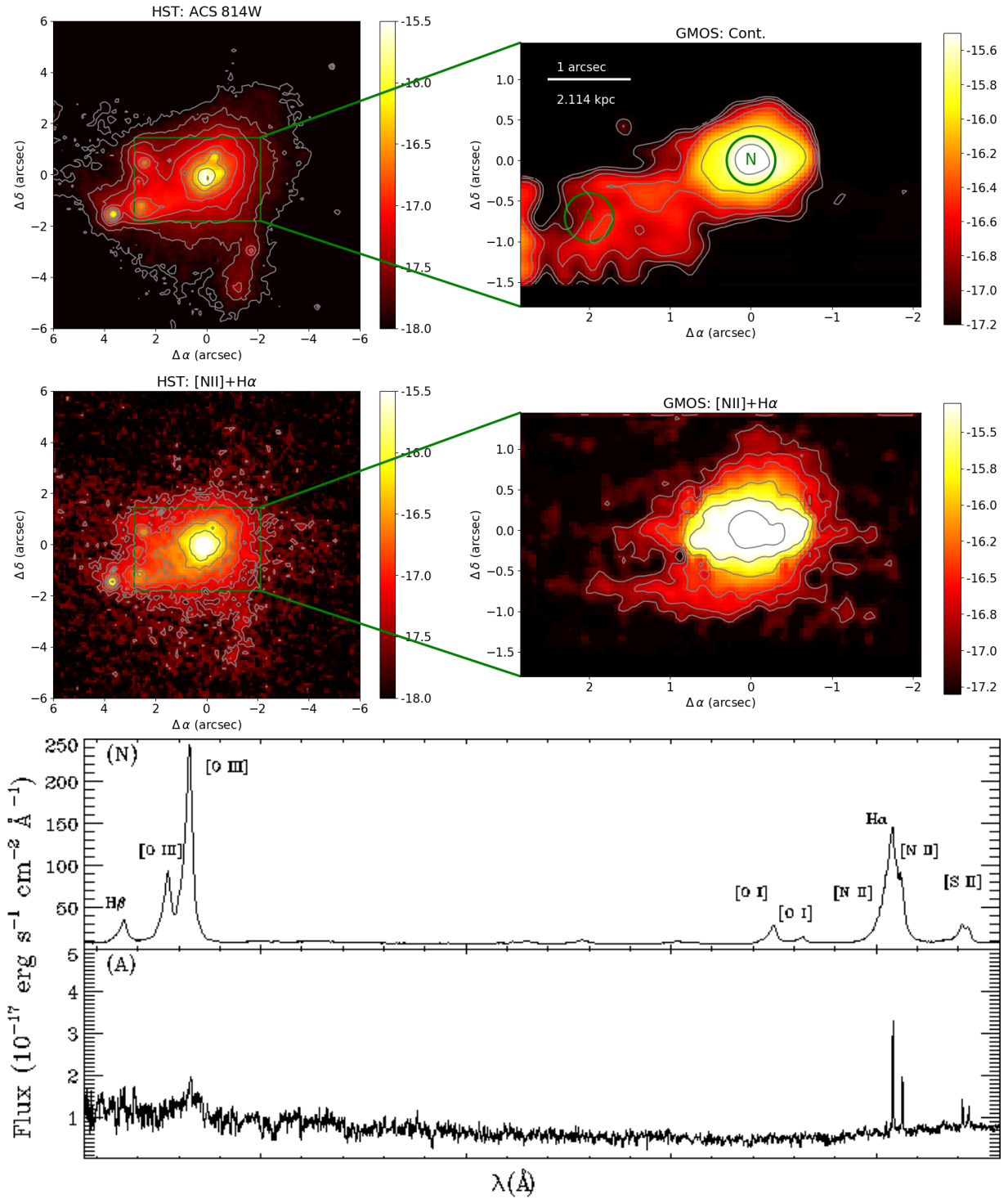


Figure 1. Top and middle: HST and GMOS-IFU images of IRAS 19154. The top and middle left panels correspond to the HST/ACS F814W - i band image of the galaxy and the HST H α + [N II] $\lambda\lambda$ 6548, 84 narrow-band image, respectively. The top and middle right panels show the corresponding GMOS-IFU continuum image within a spectral window 5500–6000 \AA (top) and another window covering the H α + [N II] $\lambda\lambda$ 6548, 84 emission lines (bottom), respectively. The color bars show the continuum in logarithmic units of $\text{erg s}^{-1} \text{cm}^{-2} \text{\AA}^{-1} \text{arcsec}^{-2}$ and the H α + [N II] $\lambda\lambda$ 6548, 84 fluxes in logarithmic units of $\text{erg s}^{-1} \text{cm}^{-2} \text{\AA}^{-1} \text{arcsec}^{-1}$. The gray contours represent levels of flux from each image, with the aim of enhancing fainter structures. The bottom plots show two representative spectra of the different regions probed by our observations: the nucleus (N), that shows broad components in the emission lines, and a region with no evidence of broad component (A). These regions are identified in the GMOS continuum image.

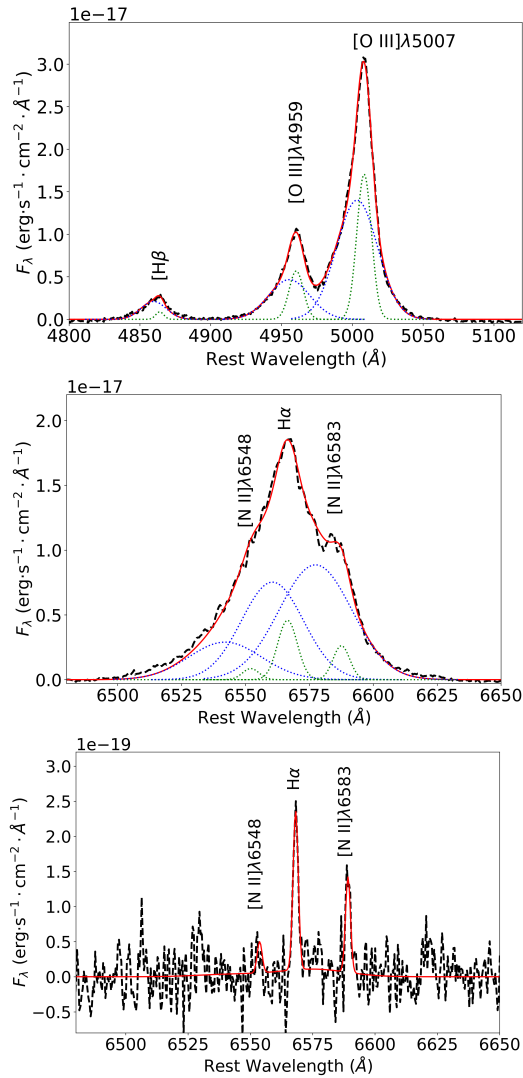


Figure 2. Examples of fits of the [O III]+H β (top panel) and [N II]+H α (middle panel) emission line profiles for the nuclear spectrum and for a position at ($0''75$ S, $2''0$ E) of the nucleus (bottom panel). The nuclear spectrum was fitted by two Gaussian curves per emission-line, while a single component per line reproduces the extra-nuclear profiles. In each panel, the observed spectrum is shown as a dashed black line and the model is shown in red. The individual Gaussian components for the nuclear profiles are shown as dotted lines in blue for the broad component and in green for the narrow component. In both panels, the spectra are continuum subtracted.

nuclear spaxel in the top and middle panels, respectively. As can be noticed, both *narrow* and *broad* Gaussian components are required to fit the emission-line profiles at the nuclear region of IRAS 19154. The bottom panel shows the fit of the H α + [N II] $\lambda\lambda$ 6548, 6583 profiles extracted at the region labelled as A in Fig. 1, separated from the nucleus by ~ 2 arcsec, for which the emission-line profiles are well represented by a single Gaussian component, narrower than that of the *narrow* component of the nuclear spectrum.

2.3 HST data

The HST images were obtained as part of a snapshot survey program designed to observe a sample of OHMGs. The observations were performed using the Advanced Camera for Surveys (ACS) with

broad (F814W), narrow (FR656N) and medium-band (FR914M) filters. The data reduction followed the standard procedure for HST images and more details can be seen in Sales et al (2015, 2019).

We have used F814W filter in order to examine the host galaxy structure. The ramp filter images were acquired for the purpose of investigating the distribution of ionized gas. The central wavelengths were configured to encompass H α in the narrow-band filter and the adjacent continuum for continuum subtraction in the medium-band filter. The bandpass of the FR656N ramp filter encompasses FR914M as well as the H α and the [N II] $\lambda\lambda$ 6548, 83 lines. The total integration times in the F814W, FR914M and narrow H α FR656N filters were 600, 200, and 600 seconds, respectively.

The pipeline image products were further processed with the IRAF¹ task *lacosim* (van Dokkum 2001) to remove cosmic rays. The continuum-free H α + [N II] image for IRAS19154 was generated using a well-established procedure. This method initially calculates the count rates for several foreground stars in both the medium (FR914M) and narrow-band (FR656N) ramp filter images (see Hoopes et al. 1999; Rossa & Dettmar 2000, 2003; Sales et al 2015). The subsequent step involved determining the mean scaling factor based on the count rate ratios. This factor was then applied to the medium-band FR914M image, which was subsequently subtracted from the narrow-band FR656N image. The continuum-subtracted H α + [N II] image was examined carefully to ensure that there were no significant residuals at the locations of the foreground stars in the image. The uncertainties associated with this method are usually $\sim 5 - 10\%$ (see Hoopes et al. 1999; Rossa & Dettmar 2000, 2003).

2.4 VLA Radio Continuum data

IRAS 19154 has been observed as part of the Karl G. Jansky Very Large Array Sky Survey (VLASS Lacy et al. 2020) at 3.0 GHz. A point source is observed with a peak intensity of 29.5 ± 0.1 mJy beam⁻¹ and an integrated flux density of $\sim 30.7 \pm 0.2$ mJy (see Fig. 3). These estimates were obtained using the AIPS Gaussian-fitting task JMFIT. The similarity in the peak and integrated values indicates that the radio source is compact. The VLASS epoch 1.2 image from May 17, 2019, has a synthesized beam size of $2.66'' \times 2.45''$ at a position angle of -89.5° . The *rms* noise in the image is 0.14 mJy beam⁻¹. JMFIT further indicates that the beam-deconvolved size of the radio source is only $\sim 0.8''$.

IRAS 19154 has also been observed as part of the NRAO VLA Sky Survey (NVSS) at 1.4 GHz on May 16, 1995 (Condon et al. 1998), where a point source is detected with a peak intensity of 61.6 ± 0.5 mJy beam⁻¹ and an integrated flux density of $\sim 64.9 \pm 0.9$ mJy. The NVSS image has a beam-size of $45'' \times 45''$, and the *rms* noise in the image is 0.43 mJy beam⁻¹. From a comparison of the NVSS and VLASS images it is evident that $\gtrsim 50\%$ of the radio emission emerges from a $\sim 0.8''$ -scale region. The peak intensities in the NVSS image and in the VLASS image after convolution with the NVSS beam of $45''$ indicates a $1.4 - 3.0$ GHz spectral index of -0.85 ± 0.15 ($S_\nu \propto \nu^\alpha$). This value is consistent with synchrotron emission and inconsistent with free-free emission. Moreover, the brightness temperature of the radio component (see Ulvestad et al. 2005) is $\sim 1.0 \times 10^4$ K, which is similar to that observed

¹ IRAF is distributed by the National Optical Astronomy Observatory, which is operated by the Association of Universities for Research in Astronomy (AURA), Inc., under cooperative agreement with the National Science Foundation.

in arcsecond-scale observations of other radio-quiet AGN (Kukula et al. 1998; Berton et al. 2018).

3 RESULTS

3.1 HST images

The upper-left and central-left panels of Figure 1 present the ACS/HST F814W *i*-band and the narrow-band $H\alpha + [N II]\lambda\lambda 6548, 6584$ images of IRAS 19154, respectively. The right panels show the corresponding GMOS-IFU images.

The *i*-band image shows the emission peak at the nucleus. This emission structure is more elongated towards the east, with three unresolved knots of enhanced emission at $\approx 1-4''$ from the nucleus, in the elongated structure. Moreover there is a faint elongation to the south of the nucleus. The GMOS continuum image, shown in the top-right panel of Figure 1, was obtained by computing the mean fluxes between 5500Å and 6000Å, a spectral region free of strong emission lines. It shows a similar elongated structure to the east as observed in the HST image, but the emission knots seen in the HST images are less evident. By convolving the HST image with a Gaussian kernel with a sigma corresponding to the seeing of the GMOS observations, the emission knots disappear. This indicates that the knots of emission are not seen in the Gemini data due to the poorer angular resolution of GMOS compared to HST.

The HST continuum-free $H\alpha + [N II]\lambda\lambda 6548, 6584$ narrow-band image, presented in the central left panel of Fig 1, shows a similar flux distribution to that of the continuum *i*-band image (top-left panel), showing similar centrally peaked emission and knots to the east of the nucleus. There is also some emission in the faint elongation to the south. A similar structure is observed in the GMOS *pseudo-narrow band* image, obtained by integrating the fluxes in the $H\alpha + [N II]\lambda\lambda 6548, 6584$ region and subtracting the continuum from adjacent regions.

3.2 GMOS – Emission-line flux distributions and kinematics

The left panels of Figure 4 present the flux distributions for the $H\alpha$ and $[O III]\lambda 5007$ emission lines. The top two panels show the maps for the narrow components and the bottom two present the maps for the broad components. The flux maps for $[O I]\lambda 6300$, $[N II]\lambda 6584$, $[S II]\lambda 6717$, and $H\beta$ are shown in Figure 5, with the results for the narrow components shown in the top panels and those for the broad components in the bottom panels.

For all emission lines, the peak flux is observed at the nucleus of the galaxy. The emission of the broad line components is restricted to an elongated structure oriented along the east-west direction, extending up to $\approx 1''$ (2.11 kpc at the galaxy) of the nucleus. The maps for the narrow components exhibit a similar emission structure at the highest flux levels, but narrow emission lines are also observed farther away from the nucleus. The most extended emission is observed for $H\alpha$ with elongated structures seen to the south-east and to the south, similarly to the larger scale emission structures observed in the HST narrow band image (Fig. 1). A similar structure, but with decreasing extent is followed by $[N II]\lambda 6583$, $[O III]\lambda 5007$, and $[S II]\lambda 6717$, covering up to $3''$ (6.3 kpc at the galaxy) of the FoV, while for $[O I]\lambda 6300$ and $H\beta$ the emission is restricted to the central $\sim 1''$ radius.

The central panels of Fig. 4 present the line of sight velocity fields for the $H\alpha$ and $[O III]\lambda 5007$ emission lines. The top two panels display the results for the narrow components, while the bottom two

panels present the velocity fields of the broad components. The color bars show the velocities in units of km s^{-1} . In all panels the systemic velocity of the galaxy, of 29975 km s^{-1} , obtained by modeling the velocity field is already subtracted. We do not present the maps for the other emission lines because they resemble those of $H\alpha$.

The velocity fields of the narrow components present a velocity gradient of $\pm 100 \text{ km s}^{-1}$ with redshifts to the southeast and blueshifts to the northwest. The $H\alpha$ velocity field (narrow component) is dominated by a rotation pattern; a similar pattern is followed by the other low-ionization lines. The narrow component of $[O III]\lambda 5007$, on the other hand, shows evidence of more disturbed kinematics. In particular, blueshifts of up to 200 km s^{-1} are observed to the north of the nucleus.

The velocity maps for the broad components present only blueshifts for all emission lines, with much higher velocity values than observed for the narrow components, reaching up to -500 km s^{-1} .

The right panels of Fig. 4 present the velocity dispersion (σ) maps (corrected for the instrumental broadening) for the narrow (top two panels) and broad (bottom two panels) components of the $H\alpha$ and $[O III]\lambda 5007$ emission lines. The narrow component presents σ values ranging from 50 to 300 km s^{-1} with the highest values observed within the inner arcsecond (2.11 kpc) for all the emission lines. Overall higher values are seen for $[O III]\lambda 5007$, as compared to lower ionization emission lines. The lowest σ values, of $\sim 50 \text{ km s}^{-1}$, are seen for $H\alpha$, and are mostly observed to the east at distances greater than 1 arcsec from the nucleus. The σ maps for the broad component present values reaching up to 900 km s^{-1} .

3.3 GMOS – Emission-line ratios and diagnostic diagrams

The top panels of Figure 6 present the $[O III]\lambda 5007/H\beta$ versus $[N II]\lambda 6584/H\alpha$ diagnostic diagram (BPT diagram; Baldwin, Phillips & Terlevich 1981), plotting each spaxel of the GMOS-IFU data obtained from the narrow components of the emission lines (left). The corresponding line-ratio maps $[O III]\lambda 5007/H\beta$ (middle) and $[N II]\lambda 6584/H\alpha$ (right) are also shown. The combination of these line ratio maps and diagnostic diagram allows us to investigate the nature of the gas excitation at each spaxel as being due to AGN or Starburst radiation or if it is due to a composite or transition between the two. The dashed and continuous curves represent the Kauffmann et al. (2003) and Kewley et al. (2006) criteria, respectively, that delimit the transition region. Each spaxel within the field of view corresponds to a point in this diagram. The dotted line, from Cid Fernandes et al. (2010), separates the regions occupied by LINERs and strong AGN (e.g. Seyfert nuclei), respectively. As the $H\beta$ emission is detected only within the inner ~ 1 arcsec (2.11 kpc) in radius around the nucleus, the BPT diagram is limited to this region. The line ratios from almost all spaxels included in the BPT diagram are located in the region occupied by strong AGN. However, in regions farther away from the nucleus than ~ 1 arcsec, the $[N I]\lambda 6584/H\alpha$ map shows values consistent with gas excitation by young stars, with $\log [N II]\lambda 6584/H\alpha < -0.2$. The bottom panels of Fig. 6 present the BPT diagram and flux line ratio maps for the broad component, showing line ratios typically observed in strong AGN.

In Figure 7 we present the visual extinction (A_V ; left panels) and electron density (N_e ; right panels) maps for the narrow (top panels) and broad components (bottom panels). The A_V values were estimated using the observed ($H\alpha/H\beta$) observed ratio, and the extinction law from Cardelli, Clayton & Mathis (1989), following the procedure described in Riffel et al. (2021c). We were able to esti-

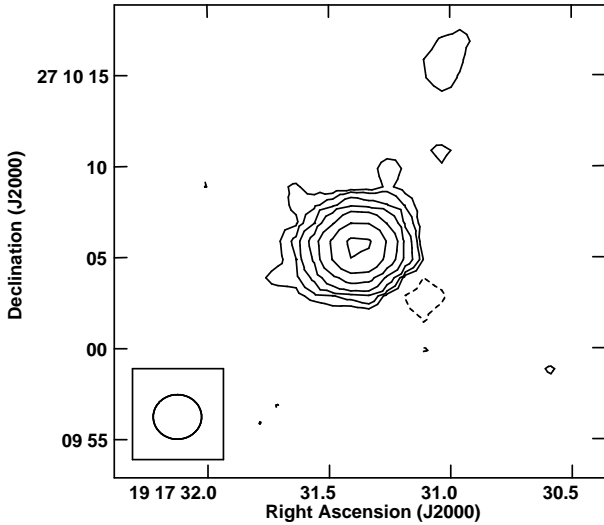


Figure 3. The VLASS image of IRAS 19154 at 3.0 GHz. A single radio component is observed. The contour levels are in percentage of the peak surface brightness ($I_p = 26.1 \text{ mJy beam}^{-1}$) and increase in steps of two with the lowest contour level being at $\pm 1.4\%$ of I_p . The beam is $2.66'' \times 2.45''$ at a position angle of -89.5° .

mate A_V only in the inner ~ 1 arcsec because the $H\beta$ emission is not detected in locations further away from the nucleus. Typical A_V values for both the broad and narrow components are in the range 1–3 mag. The mean values are 2.1 ± 1.4 mag and 1.64 ± 1.1 mag for the narrow and broad components, respectively. The quoted errors correspond to the standard deviation of the mean values.

The $[\text{N II}]\lambda 5755$ line is detected in the nuclear spectrum, allowing us to use the $[\text{N II}]\lambda 6548, 6583/[\text{N II}]\lambda 5755$ line ratio to estimate the electron temperature. Taking the line fluxes measured within a circular aperture of $0''.3$ radius, roughly corresponding to the seeing of the GMOS observations, we find $T_e \approx 19000 \pm 4000$ K using the PYNEB code. This temperature value is slightly larger than the values commonly reported for AGN photoionized gas ($T_e \approx 15000$ K; Dors et al. 2017, 2020; Revalski et al. 2018, 2021; Riffel et al. 2021b), but still lower than shock dominated regions ($T_e \gtrsim 25000$ K; Riffel et al. 2021a). We estimate N_e from the $[\text{S II}]\lambda 6717/\lambda 6731$ line ratio using the PYNEB code (Luridiana, Morisset & Shaw 2015), adopting an electron temperature of 19000 K. The N_e maps for the narrow and broad components are shown in the top and bottom right panels of Fig. 7, respectively. Typical N_e values for both the broad and narrow components fall in the range from ~ 200 to $\sim 1300 \text{ cm}^{-3}$ with the highest values observed within the inner 1 arcsec in radius from the nucleus, while the lowest values are seen mostly at greater distances. The mean values for the narrow and broad components are 580 ± 370 and $1110 \pm 520 \text{ cm}^{-3}$, respectively.

4 DISCUSSION

4.1 Gas kinematics and outflows

The emission-line profiles in IRAS19154 are well reproduced by two Gaussian functions. And in this case, we assume that the broad and narrow components are measuring properties of different groups of clouds. In this section we discuss the main characteristics of the regions emitting these components.

4.1.1 The narrow component

The gas velocity fields for the narrow components show mostly redshifts to the southeast and blueshifts to the northwest at least for distances larger than ~ 1 arcsec – that is, distances greater than 2.1 kpc at the galaxy. This behaviour suggests that the narrow component velocities, at least from these regions, are consistent with rotation in the galaxy plane. Within the inner 2.1 kpc, distortions from pure rotation are observed, as a twist in the zero velocity curve seen in $H\alpha$ and the blueshifts observed in the $[\text{O III}]\lambda 5007$ velocity field.

To characterize the velocity field, we employ an analytical model, assuming that the gas follows circular orbits within the galactic plane, where the circular velocity is described by (van der Kruit & Allen 1978; Bertola et al. 1991),

$$V_{\text{mod}}(R, \psi) = V_s +$$

$$\frac{AR \cos(\psi - \psi_0) \sin(i) \cos^p(i)}{\{R^2[\sin^2(\psi - \psi_0) + \cos^2(i) \cos^2(\psi - \psi_0)] + c_0^2 \cos^2(i)\}^{\frac{p}{2}}}, \quad (1)$$

where R is the distance from the nucleus projected on the plane of the sky and ψ is its corresponding position angle; V_s is the systemic velocity of the galaxy; A is the velocity amplitude; i is the inclination of the disc relative to the plane of the sky; ψ_0 is the orientation of the line of nodes, measured North through East; c_0 is a concentration parameter, defined as the radius where the rotation curve reaches 70% of the velocity amplitude; and the parameter p measures the slope of the rotation curve beyond the maximum amplitude.

Figure 8 shows the observed velocity field for the $H\alpha$ narrow component in the left panel, the best-fit model in the central panel, and the residual map obtained by subtracting the model from the observed velocity field is shown in the right panel. At most locations, the residual velocities are smaller than $\sim 40 \text{ km s}^{-1}$, indicating that the majority of the narrow component emitting gas is rotating in the galaxy plane. The kinematical centre located at $(\Delta\alpha, \Delta\delta) = (0''.25, 0''.15)$ is slightly displaced from the position of the continuum peak. The disc kinematic major axis is oriented along the position angle $\Psi_0 \approx 96^\circ$ and the derived systemic velocity is $\approx 29975 \text{ km s}^{-1}$. The highest velocity residuals are mostly observed within the inner 1 arcsec, where distinct behaviours are observed for the gas velocity field of the high ionization (traced by the $[\text{O III}]\lambda 5007$ emission) and the low ionization (traced by $H\alpha$ and other emission lines) gas. The highest ionization gas is blueshifted by about 100 km s^{-1} , while the low ionization gas presents velocities close to zero in the central region. This result suggests that part of the gas emitting the narrow component is also outflowing, as is the case for the gas emitting the broad component, discussed in the next section. A puzzling velocity residual pattern is observed approximately 1 arcsec (2.1 kpc) east/southeast of the nucleus, suggesting a compact rotation pattern, that may be related with the interaction being suffered by this galaxy.

The velocity dispersion values for the narrow component (Figure 4) are in the range from 50 to 350 km s^{-1} , with the highest values being observed for the highest ionization gas within the inner arcsec and co-spatial with the locations where the $[\text{O III}]\lambda 5007$ velocity field shows blueshifts. This is also co-spatial with the region where the broad component is detected. This indicates that the distortions relative to pure rotation in the inner region of IRAS19154 may be due to a disturbance of the gas in the plane of the disc by an outflow, traced by the broad component.

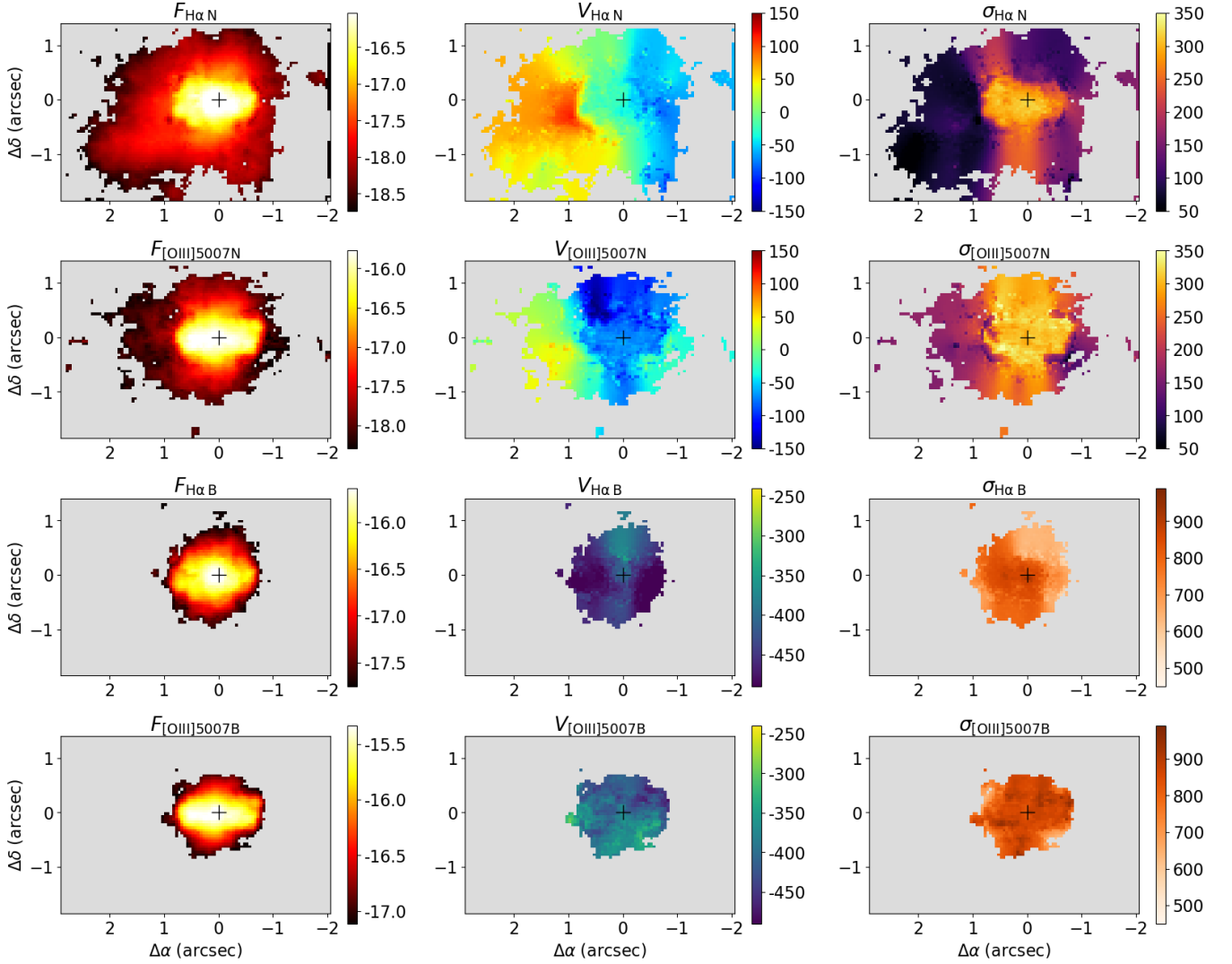


Figure 4. Flux distributions and kinematics for the $[\text{O III}]\lambda 5007$ and $\text{H}\alpha$ emission lines of IRAS19154, based on the GMOS data. The left column displays the flux distributions, for the $\text{H}\alpha$ narrow component, $[\text{O III}]\lambda 5007$ narrow component, $\text{H}\alpha$ broad component, and $[\text{O III}]\lambda 5007$ broad component, from top to bottom. The central column shows the corresponding line of sight velocity fields and the right column presents the velocity dispersion maps. In all panels the central crosses mark the position of the nucleus and grey regions indicate masked locations where signal-to-noise was not high enough to allow measurements or locations with no detection of line emission. The color bars show the fluxes in logarithmic units of $\text{erg s}^{-1} \text{cm}^{-2} \text{spaxel}^{-1}$ and the velocities and velocity dispersions in km s^{-1} . The velocity fields are shown after correction for the systemic velocity of the galaxy and the σ maps are corrected for instrumental broadening.

4.1.2 The broad component

The velocity fields derived from the broad component show essentially blueshifts for all emission lines, with values reaching about -500 km s^{-1} . These features are observed within the inner 2.1 kpc and are consistent with outflows. All velocity values are negative, indicating that the gas is mostly coming towards us. AGN outflows in ionized gas are usually bi-polar, but we do not see the redshifted counterpart of the blueshifted outflow. We attribute this result as due to the fact that the redshifted outflow is hidden behind the galaxy plane due extinction by dust.

The observed velocity fields can thus be understood as follows. The broad component – which is strongly blueshifted, represents a strong disturbance in the gas kinematics that can be attributed to the presence of an AGN driven wind. The narrow component could in-

stead originate in gas clouds that are less affected by the presence of the nuclear outflow. The narrow component may be tracing the emission of the gas in the galaxy potential which is not strongly affected by the outflow in regions away from nucleus, while in the central arcsec the passage of the wind increases the turbulence of the gas in the host galaxy. Under the assumption that the broad component is due to an AGN driven outflow, we can now estimate its properties.

4.1.3 Outflow properties

We can estimate the mass outflow rate as being the ratio of the mass of the outflowing gas to the dynamical time for the gas to reach its present position. The mass of outflowing gas can be estimated by

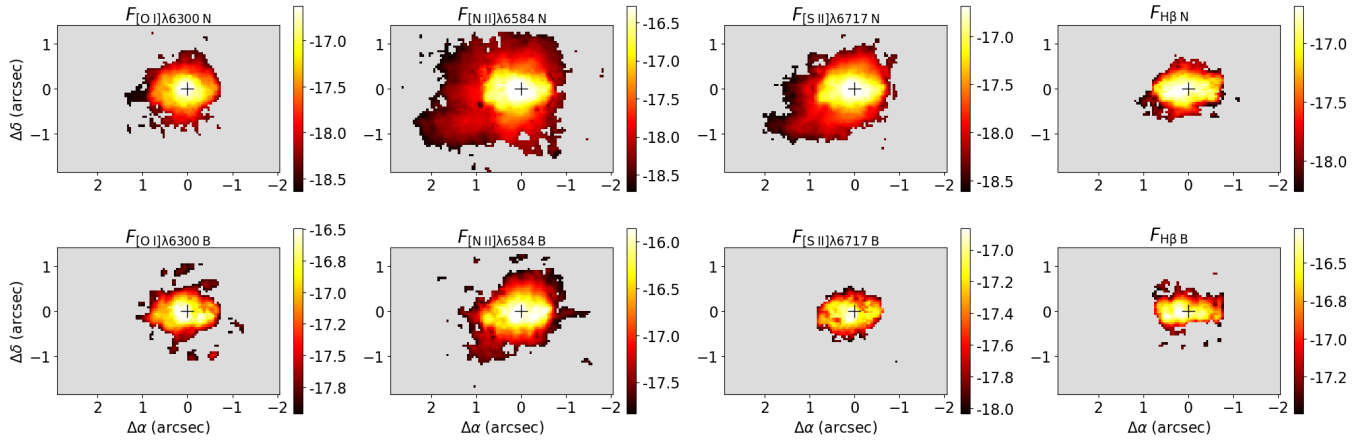


Figure 5. Emission-line flux distributions for the narrow (top) and broad (bottom) components, based on GMOS data. The maps for [O III]λ6300, [N II]λ6584, [S II]λ6717 and Hβ are shown from left to right. In all panels the central crosses mark the position of the nucleus and grey regions indicate masked locations where signal-to-noise was not high enough to allow measurements or locations with no detection of line emission. The color bars show the fluxes in logarithmic units of $\text{erg s}^{-1} \text{cm}^{-2} \text{spaxel}^{-1}$.

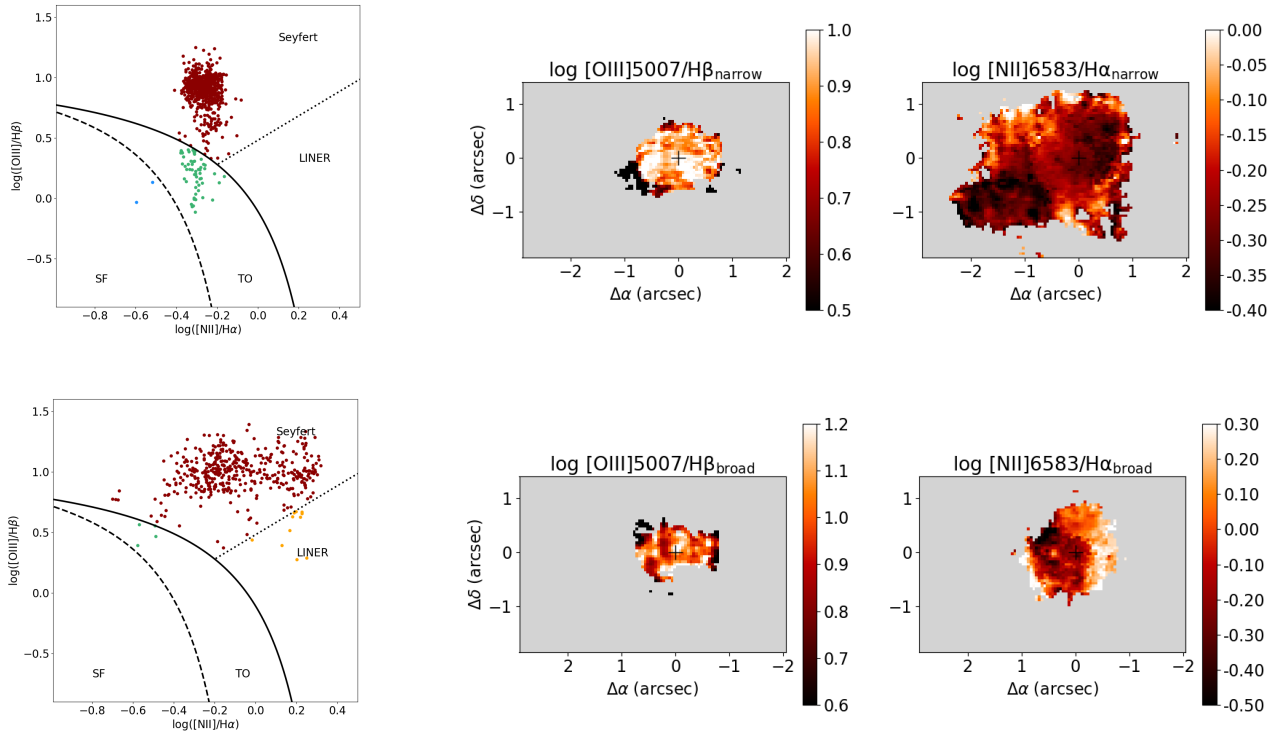


Figure 6. Top panels: $\log [\text{O III}]\lambda 5007/\text{H}\beta$ versus $\log [\text{N II}]/\text{H}\alpha$ diagnostic diagram of IRAS19154 obtained from its narrow components. $\log [\text{O III}]/\text{H}\beta$ (middle) and $\log [\text{N II}]\lambda 6583/\text{H}\alpha$ line ratio maps (right). The dashed, continuous and dotted curves represent the borderlines from [Kauffmann et al. \(2003\)](#), [Kewley et al. \(2006\)](#) and [Cid Fernandes et al. \(2010\)](#), respectively. Bottom panels: Same as top panels, but using the fluxes of the broad components of the emission lines.

$$M_g = N_e m_p V f \quad (2)$$

$$L_{H\alpha} \approx f N_e^2 j_{H\alpha}(T) V, \quad (3)$$

where N_e is the electron density, m_p is the mass of the proton, V is the volume of the region where the outflow is observed and f is the filling factor that can be estimated from

where $j_{H\alpha} = 3.3534 \times 10^{-25} \text{ erg cm}^{-3} \text{ s}^{-1}$ ([Osterbrock & Ferland 2006](#)) and $L_{H\alpha}$ is the $\text{H}\alpha$ luminosity emitted within the volume V .

Combining the above equations, we obtain

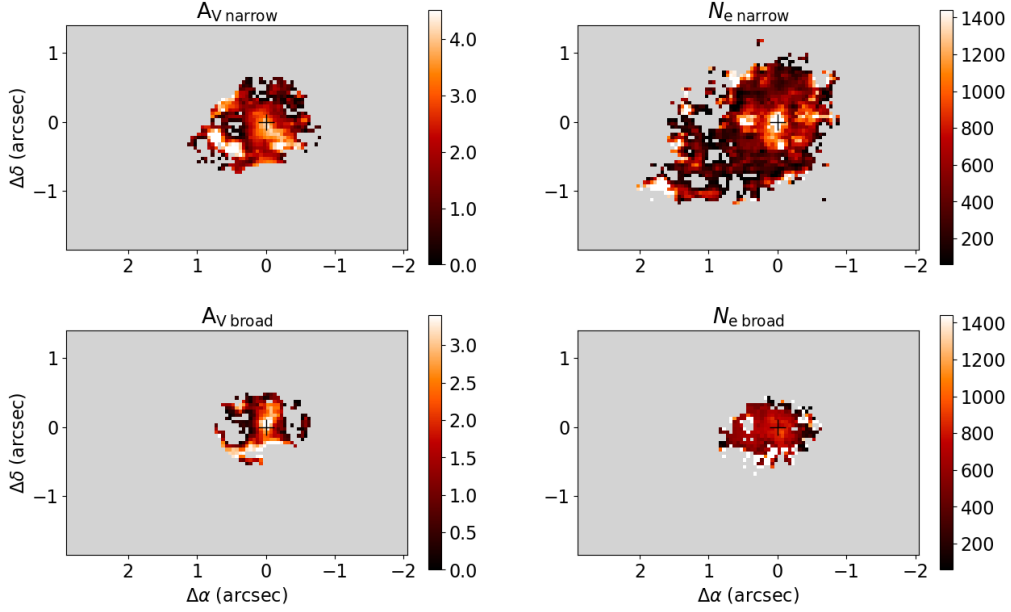


Figure 7. Visual extinction (left), derived from the $H\alpha/H\beta$ line ratio, and electron density (right) maps, obtained from the $[S\ II]\lambda\lambda 6717, 6731$ fluxes, for the narrow (top) and broad (bottom) components. The color bars show the visual extinction in magnitudes and the electron density in cm^{-3}

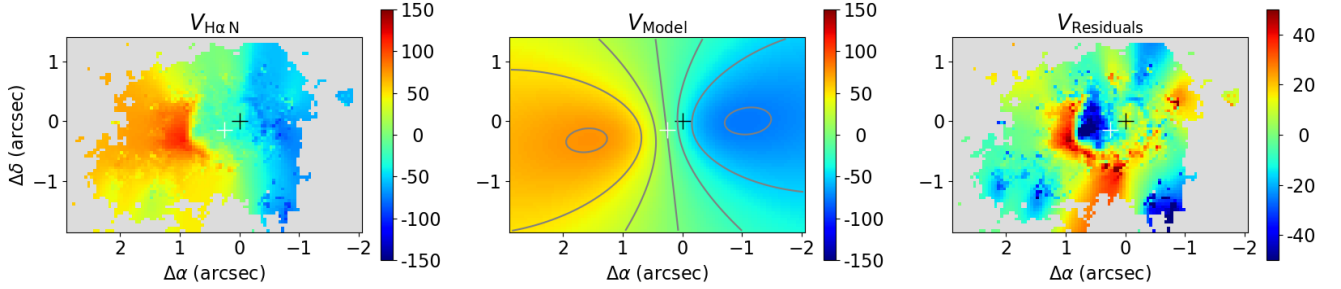


Figure 8. Observed $H\alpha$ velocity field for the narrow component (left), rotating disc model (centre) and residual map (right), defined as the difference between the observed velocities and the model. The black crosses mark the position of the nucleus, while the white crosses show the location of the kinematical centre.

$$M_g = \frac{m_p L_{H\alpha}}{N_e j_{H\alpha}(T)}. \quad (4)$$

We estimate the observed $H\alpha$ luminosity of the outflow component by summing up the $H\alpha$ fluxes of the broad, blueshifted component of all spaxels and adopting a luminosity distance to IRAS19154 of 436 Mpc. We obtain $L_{H\alpha, \text{obs}} = (8.9 \pm 0.4) \times 10^{41} \text{ erg s}^{-1}$. Using the extinction law from [Cardelli, Clayton & Mathis \(1989\)](#) and the mean visual extinction of $A_{V, \text{out}} = 1.6 \pm 0.7$ for the outflow (Fig. 7), the resulting extinction corrected $H\alpha$ luminosity of the outflow is $L_{H\alpha} = (3.0 \pm 1.4 \times 10^{42} \text{ erg s}^{-1})$. To estimate the mass of ionized hydrogen, we use an average density for the outflowing gas of $N_e \approx 1110 \text{ cm}^{-3}$ obtained from the $[S\ II]$ doublet (Fig. 7). The resulting mass is $M_g = (6.7 \pm 3.1) \times 10^6 M_\odot$.

To estimate the dynamical time, we assume a radius of $0''.4$ ($\approx 850 \text{ pc}$), which corresponds to half of the full width at half maximum of the flux distribution of the broad component of $[O\ III]\lambda 5007$, and an outflow velocity of $V_{\text{out}} \approx 500 \text{ km s}^{-1}$ obtained from the centroid velocity of the broad emission-line component (Fig. 4). Under these assumptions, the resulting mass-outflow rate is $\dot{M}_{\text{out}} = 4.0 \pm 2.6 M_\odot \text{ yr}^{-1}$, which is consistent with the values obtained for

AGN with luminosities similar to that of IRAS19154 (e.g. [Kakkad et al. 2022](#); [Deconto-Machado et al. 2022](#); [Riffel et al. 2023](#)).

We now compare the mass outflow rate with the mass accretion rate needed to feed the SMBH, which can be estimated as

$$\dot{M}_{\text{acc}} = \frac{L_{\text{bol}}}{\eta c^2}, \quad (5)$$

where L_{bol} is the bolometric luminosity and c is the light speed. We estimate the bolometric luminosity from the observed $[O\ III]\lambda 5007$ luminosity of the broad component, $L_{[O\ III]} \approx 2.2 \times 10^{42} \text{ erg s}^{-1}$, using the relation $L_{\text{bol}} = 3500 L_{[O\ III]}$ ([Heckman et al 2004](#)). This yields $L_{\text{bol}} \approx 7.8 \times 10^{45} \text{ erg s}^{-1}$. Assuming the radiative efficiency $\eta = 0.1$, we derive a mass accretion rate of $1.4 M_\odot \text{ yr}^{-1}$. Thus, the mass outflow rate in ionized gas is roughly 3 times larger than the accretion rate necessary to fuel the AGN.

The kinetic power of the ionized gas outflow can be estimated by

$$\dot{E}_{\text{out}} = \frac{1}{2} \dot{M} (V_{\text{out}}^2 + 3\sigma_{\text{out}}^2) \quad (6)$$

where V_{out} and σ_{out} are the outflow velocity and its velocity dispersion. Using $V_{\text{out}} \approx 500 \text{ km s}^{-1}$ and $\sigma_{\text{out}} \approx 750 \text{ km s}^{-1}$ (Fig. 4)

the resulting kinetic power of the outflow is $\dot{E}_{\text{out}} = (2.5 \pm 1.6) \times 10^{42} \text{ erg s}^{-1}$.

Comparing the kinetic power with the bolometric luminosity, we find that $\dot{E}_{\text{out}}/L_{\text{bol}}$ is about 3×10^{-4} . This value is lower than the outflow coupling efficiencies required by cosmological simulations for AGN feedback to become effective in suppressing star formation in the host galaxy (Hopkins & Elvis 2010; Harrison et al. 2018). However, one may consider that this kinetic efficiency corresponds only to the mechanical effect of the outflow seen in a specific gas phase and not to the total AGN energy. Indeed, recent theoretical results indicate that low-power outflows can be efficient in quenching star formation in the host galaxy, if sustained for at least ~ 1 Myr (Almeida et al. 2023).

We note that, at a mass-outflow rate of $4M_{\odot} \text{ yr}^{-1}$, it will take only ≈ 0.25 Myr for all the ionized gas mass emitting the broad component to be expelled. If the outflow duration is, for example, 10 Myr (assuming that the outflow is active for $\approx 10\%$ of a typical 100 Myr AGN lifecycle; Schawinski et al. 2015), $\approx 10^8 M_{\odot}$ would be ejected during the activity cycle, in ionized gas alone.

4.2 Scenario and comparison with previous studies

The HST images in Fig. 1 show that IRAS 19154 is very irregular, with clear signatures of interaction, although no separate companion is seen in the images, indicating that the interaction is in an advanced stage. This interaction is the most probable trigger of the AGN. This galaxy is part of a larger sample of interacting galaxies, selected from Darling & Giovanelli (2000), for which we are conducting detailed studies based on observations at multiple wavelengths. All the galaxies included in the sample present OH megamaser emission, except for IRAS 19154. Four out of the five galaxies studied previously exhibit clearer signs of interaction, when one can see the two components, and the presence of AGNs (except for IRAS 17526+3253). However, IRAS 19154 is the first object to show, besides the gas excitation by an AGN, clear high-velocity outflows. It is possible that the outflows begin when the interaction is in an advanced stage, but a larger sample will be needed to investigate this question.

In order to compare our results for IRAS 1915 with those for our other studies of OHM galaxies, we now summarize our previous results. In Sales et al (2015), a multiwavelength analysis of IRAS 16399-0937 revealed an embedded AGN in the northwestern nucleus of the galaxy. Another AGN was found in the galaxy IRAS 23199+0123 which is a clear interacting pair of galaxies, a study in which we reported a new OH maser detection and related the maser sources to shocks driven by the AGN outflows (Hekatelyne et al 2018a). Our study of IRAS 03056+2034 revealed the presence of a circumnuclear star formation ring, in the center of which the BPT diagram and VLA data suggest the presence of another embedded AGN that is responsible for the gas excitation together with the star forming regions (Hekatelyne et al 2018b). IRAS 11506-3851 shows star-forming regions surrounding the nucleus but the multi wavelength analysis also suggests the presence of an embedded AGN (Hekatelyne et al 2020). The only OHM galaxy for which we did not find evidence for the presence of an AGN is IRAS 17526+3253, which hosts a H_2O maser and shows only excitation by star-forming regions, although a more comprehensive study may be necessary to confirm this result (Sales et al 2019).

The study of the above OHM galaxies shows a repeated pattern where star forming regions surround the nucleus, which itself shows evidence of the presence of an AGN. In addition, all these galaxies present signatures of interactions in the recent past or are clearly in

a merger process. Three of these galaxies are mergers and three of them are the result of a recent merger event and for most of them the data suggest the presence of an embedded AGN.

We note that, although our sample of studied galaxies is still small, we tentatively identify a trend where the AGN is more evident in galaxies that are in a more advanced merger stage, as well as its impact in the host galaxy, such as the outflows seen in IRAS 1915. And in these cases the contribution of the AGN to the gas excitation is increased relative to that of the starburst activity. In the particular case of IRAS 19154 (and others in an advanced merger stage), it seems that the AGN has already become powerful enough to produce outflows in ionized gas; in this environment, it is less likely that new stars will form close to the nucleus, but they may be observed farther out.

5 CONCLUSIONS

We have presented a two-dimensional study of the inner $6 \text{ kpc} \times 4 \text{ kpc}$ region of the OH absorber galaxy IRAS 19154 using GMOS - IFU observations. Our aim was to map its gas distribution and kinematics, as well as to determine its excitation mechanism. We summarize our main conclusions as follows:

- Within the inner $\approx 2 \text{ kpc}$ radius, the gas presents two kinematic components: a broad component with velocity dispersion $500 \lesssim \sigma \lesssim 900 \text{ km s}^{-1}$ and a narrow component with $50 \leq \sigma \leq 350 \text{ km s}^{-1}$, while in the outer regions, only the narrow component is observed;
- We attribute the broad component to an AGN driven outflow, with velocities ranging from -350 to -500 km s^{-1} . The outflow component is observed only in blueshifts, while the redshifted counterpart is probably obscured by the disc of the galaxy;
- We attribute the narrow component to gas orbiting in the galaxy potential. Its velocity field is well reproduced by a rotating disk model at distances larger than $\sim 2 \text{ kpc}$ from the nucleus. A mild increase in the velocity dispersion and a higher discrepancy between the rotating disk model and the observed velocities are seen in the central region, co-spatial with the detection of the outflow component. This suggests that the gas in the disc is disturbed either by the outflows or the interaction that this galaxy is undergoing;
- The analysis of the emission line ratios reveals a powerful AGN ionizing and exciting the gas in the outflow, as well as the gas in the disc within the inner $\sim 2 \text{ kpc}$ radius. Regions of low $[\text{N II}]\lambda 6584/\text{H}\alpha$ are seen farther away, indicating gas emission associated with star forming regions. This is further supported by the detection of emission knots in the HST images in the continuum and $\text{H}\alpha$, beyond this region;
- The mass of ionized gas in the outflow is $\approx 6.7 \times 10^6 M_{\odot}$, and the corresponding mass-outflow rate is $\dot{M}_{\text{out}} \approx 4 M_{\odot} \text{ yr}^{-1}$. We estimate a kinetic power of the outflow of $2.5 \times 10^{42} \text{ erg s}^{-1}$, which is nevertheless only $3 \times 10^{-4} L_{\text{bol}}$.
- Although the above value is lower than prescribed by models for a significant impact on the host galaxy, at a mass-outflow rate of $4 M_{\odot} \text{ yr}^{-1}$, all the present outflowing gas mass will be ejected from the central region in ~ 0.25 Myr; $\approx 10^8 M_{\odot}$ will be ejected in a ~ 10 Myr AGN lifecycle, in ionised gas alone.

The scenario we propose for IRAS 19154 is that a recent interaction has triggered the AGN and its outflow. IRAS 19154 is the 6th galaxy we have observed with GMOS-IFU and the 5th for which we have found the presence of an AGN. Unlike the previous cases, it is an OH absorber, while the others are OHM galaxies. It is also the first showing the clear presence of an AGN outflow. This supports a trend

of stronger AGN signatures in more advanced stages of interactions and mergers.

ACKNOWLEDGEMENTS

We thank an anonymous reviewer for providing valuable comments that helped us improve this paper. This work is based on observations obtained at the Gemini Observatory, which is operated by the Association of Universities for Research in Astronomy, Inc., under a cooperative agreement with the NSF on behalf of the Gemini partnership: the National Science Foundation (United States), National Research Council (Canada), CONICYT (Chile), Ministerio de Ciencia, Tecnología e Innovación Productiva (Argentina), Ministério da Ciência, Tecnologia e Inovação (Brazil), and Korea Astronomy and Space Science Institute (Republic of Korea). This research has made use of NASA's Astrophysics Data System Bibliographic Services. This research has made use of the NASA/IPAC Extragalactic Database (NED), which is operated by the Jet Propulsion Laboratory, California Institute of Technology, under contract with the National Aeronautics and Space Administration. Support for programme HST-SNAP 11604 was provided by NASA through a grant from the Space Telescope Science Institute, which is operated by the Association of Universities for Research in Astronomy, Inc., under NASA contract NAS 5- 26555. C.H. thanks CAPES for financial support. R.A.R. acknowledges the support from Conselho Nacional de Desenvolvimento Científico e Tecnológico (CNPq; Proj. 400944/2023-5 & 404238/2021-1) and Fundação de Amparo à pesquisa do Estado do Rio Grande do Sul (FAPERGS; Proj. 21/2551-0002018-0). D.A.S. also CNPq, FAPERGS and CAPES for financial support. P.K acknowledges the support of the Department of Atomic Energy, Government of India, under the project 12-R&D-TFR-5.02-0700.

DATA AVAILABILITY

The GEMINI data used in this work is publicly available online via the GEMINI archive <https://archive.gemini.edu/searchform/>, with project code GN-2017B-Q-38. The VLA data is available at <https://science.nrao.edu/facilities/vla/archive>. Finally, the HST data is available at <https://archive.stsci.edu/hst/> with project code 11604. The data cubes produced from these data can be shared on reasonable request to the corresponding author.

REFERENCES

- Allington-Smith, J. et al. 2002, *PASP*, 114, 892.
 Allen, M. G., Groves, B. A., Dopita, M. A., Sutherland, R. S. and Kewley, L. J., 2008, *ApJS*, 178, 20
 Almeida, I., Nemmen, R., Riffel, R. A., 2023, *MNRAS*, 526, 217.
 Araujo, B. L. C., Storchi-Bergmann, T., Rembold, S. B., Kaipper, A. L. P., Dall'Agnol de Oliveira, B., 2023, *MNRAS*, 522, 5165.
 Bae, H.-J., Woo, J.-H., 2016, *ApJ*, 828, 97.
 Baldwin, J. A., Phillips, M. M., Terlevich, R., 1981, *PASP*, 93, 5
 Barnes, J. E., & Hernquist, L. 1992, *ARA&A*, 30, 705
 Berton, M, 2018, *A&A*, 614, 87.
 Bertola, F., Bettoni, D., Danziger, J., Sadler, E., Sparke, L., de Zeeuw, T., 1991, *ApJ*, 373, 369
 Brum, C. et al., 2019, *MNRAS*, 486, 691
 Cardelli, J. A., Clayton, G. C., Mathis, J. S., 1989, *ApJ*, 345, 245.
 Cid Fernandes, R., Stasińska, G., Schlickmann, M. S., Mateus, A., Vale Asari, N., Schoenell, W., Sodré, L., 2010, *MNRAS*, 403, 1036.
 Condon, J. J., Cotton, W. D., Greisen, E. W., Yin, Q. F., Perley, R. A., Taylor, G. B., Broderick, J. J., 1998, *AJ*, 115, 1693.
 Dall'Agnol de Oliveira, B. et al., 2021, *MNRAS*, 504, 3890.
 Darling J., Giovanelli R., 2000, *ApJ*, 119, 3003
 Darling J., Giovanelli R., 2001, *ApJ*, 121, 1278
 Darling J., Giovanelli R., 2002, *ApJ*, 124, 100
 Deconto-Machado, A. et al., 2022, *A&A*, 659, 131.
 do Nascimento, J. C. et al, 2022, 513, 807.
 Dors, O. L., Arellano-Córdova, K. Z., Cardaci, M. V., Hägele, G. F., 2017, *MNRAS*, 468, 113.
 Dors, O. L., Maiolino, R., Cardaci, M. V., Hägele, G. F., Krabbe, A. C., Pérez-Montero, E., Armah, M., 2020, *MNRAS*, 496, 3209.
 Freitas, I. C. et al., 2018, *MNRAS*, 476, 2760.
 Haan, S., Surace, J. A., Armus, L., et al. 2011, *AJ*, 141, 100
 Harrison C. M., Costa T., Tadhunter C. N., Flüttsch A., Kakkad D., Perna M., Vietri G., 2018, *Nature Astronomy*, 2, 198
 Heckman T. M., Kauffmann G., Brinchmann J., Charlot S., Tremonti C., White S. D. M., 2004, *ApJ*, 613, 109.
 Hekatelyne, C., Riffel, R. A., Sales, D., Robinson, A., Gallimore, J., Storchi-Bergmann, T., Kharb, P., O'Dea, C. Baum, S., 2018a *MNRAS*, v. 474, p. 5319
 Hekatelyne, C., Riffel, R. A., Sales, D., Robinson, A., Storchi-Bergmann, T., Kharb, P., Gallimore, J., Baum, S., O'Dea, C., 2018b, *MNRAS*, v. 479, p. 3966
 Hekatelyne, C., Riffel, R. A., Storchi-Bergmann, T., Kharb, P., Robinson, A., Sales, D., Cassanta, C., 2020, *MNRAS*,
 Hoopes, C., G., Walterbos, R. A. M., Rand, R. J., 1999, *ApJ*, 552, 669.
 Hook, I., Jorgensen, I., Allington-Smith, J. R., Davies, R. L., Metcalfe, N., Murowinski, R. G., Crampton, D., 2004, *PASP*, 116, 425
 Hopkins, P. F., Hernquist, L., Cox, T. J., et al. 2006, *ApJS*, 163, 1
 Hopkins P. F., Elvis M., 2010, *MNRAS*, 401, 7
 Kakkad, D. et al., 2022, *MNRAS*, 511, 2105.
 Kauffmann, G. et al. 2003a, *MNRAS*, 346, 1055
 Kewley, L. J. Groves, B., Kauffmann G., Heckman, T., 2016, *MNRAS*, 372
 Krabbe, A. C. et al., 2014, *MNRAS*, 437, 1155.
 Kraemer, S. B., Ho, L. C., Crenshaw, D. M., Shields, J. C., Filippenko, A. V., 1999, *ApJ*, 520, 564.
 Kukula, M. J., Dunlop, J. S., Hughes, D. H., Rawlings, S., 1998, *MNRAS*, 297, 366
 Lacy, M., 2020, *PASP*, 132c5001L
 Lo K. Y., 2005, *ARA&A*, 43, 625
 Ludwig, R. R., Greene, J. E., Barth, A. J., Ho, L. C., 2012, *ApJ*, 756, 51
 Luridiana, V., Morisset, C., Shaw, R. A., 2015, *A&A*, 573, A42
 Mihos, J. C. 1995, *ApJ*, 438, 75.
 Nakanishi, K., Takata, T., Yamada, T., Takeuchi, T. T., Shiroya, R., Miyazawa, M., Watanabe, S., & Saito, M. 1997, *ApJS*, 112, 245
 Osterbrock, D. E., Ferland, G. J., 2006, Sausalito, CA: University Science Books.
 Perez, J. Michel-Dansac, L. Tissera, P. B., 2011, *MNRAS*, 417, 580.
 Petric, A. O. et al., 2018, *AJ*, 156, 295.
 Revalski, M., Crenshaw, D. M., Kraemer, S. B., Fischer, T. C., Schmitt, H. R., Machuca, C., 2018, *ApJ*, 856, 46.
 Revalski, M. et al., 2021, *ApJ*, 910, 139.
 Riffel, R. A. et al., 2021a, *MNRASL*, 501, L54.
 Riffel, R. A., Dors, O. L., Krabbe, A. C., Esteban, C., 2021b, *MNRASL*, 506, L11.
 Riffel, R. A. et al., 2023, *MNRAS*, 521, 1832.
 Riffel, R. et al., 2021, *MNRAS*, 501, 4064.
 Rossa, J.; Dettmar, R. -J, *A&A*, 359, 433.
 Rossa, J.; Dettmar, R. -J, *A&A*, 406, 505.
 Ruschel-Dutra D., 2020, [danielrd6/ifscube v1.0,doi:10.5281/zenodo.3945237](https://doi.org/10.5281/zenodo.3945237)
 Ruschel-Dutra D. et al., 2021, *MNRAS*, 507, 74.
 Schawinski, K., Koss, M., Berney, S., Sartori, L. F., 2015, *MNRAS*, 451, 2517.
 Schwarzkopf, U., Dettmar, R. -J., 2000, *A&A*, 361, 451.
 Sales, D. A., Robinson, A., Axon, D. J., et al., 2015, *ApJ*, 799, 25
 Sales, D., Robinson, A., Riffel, R. A, Storchi-Bergmann, T, Gallimore, J, F

- Kharb, P., Baum, S., O’dea, C., Hekatelyne, C., Ferrari, F., 2019, MNRAS, v. 486, 3350
- Sanders, D. B., Soifer, B. T., Elias, J. H., et al. 1988, ApJ, 325, 74
- Soifer, B. T. et al. 1987, ApJ, 320, 238.
- Storchi-Bergmann, T. & Schnorr-Müller, A 2019, Nature Astronomy, 3, 48
- Tissera, P. B., Domínguez-Tenreiro, R., Scannapieco, C., Sáiz, A., 2002, MNRAS, 333, 327.
- Tody, D. 1986, The IRAF Data Reduction and Analysis System in Proc. SPIE Instrumentation in Astronomy VI, ed. D.L. Crawford, 627, 733
- Tody, D. 1993, IRAF in the Nineties" in Astronomical Data Analysis Software and Systems II, A.S.P. Conference Ser., Vol 52, eds. R.J. Hanisch, R.J.V. Brissenden, J. Barnes, 173.
- Ulvestad, J. S., Wong, D. S., Taylor, G. B., Gallimore, J. F., Mundell, C. G., 2005, ApJ, 130, 936,
- van der Kruit, P.C., Allen, R.J., 1978, ARA&A, 16, 103
- Van Dokkum, P. G., 2001, PAP, 113, 789.

This paper has been typeset from a \TeX/L\AA\TeX file prepared by the author.